PCCP

ROYAL SOCIETY OF CHEMISTRY

PAPER

View Article Online
View Journal | View Issue

Cite this: *Phys. Chem. Chem. Phys.*, 2022, **24**, 26200

Rapid crystallization of amorphous solid water by porosity induction†

Gaurav Vishwakarma,[a] Bijesh K. Malla,[a] Rabin Rajan J. Methikkalam[b] and Thalappil Pradeep *[ac]

Received 10th June 2022,
Accepted 11th October 2022

DOI: 10.1039/d2cp02640f

rsc.li/pccp

Rapid crystallization of amorphous solid water (ASW) is often associated with crystallization that initiates at random nucleation sites in the bulk and expands in all directions. In this work, by preparing sandwich films of acetonitrile (ACN) and ASW in the form of ACN@ASW and ASW@ACN in an ultrahigh vacuum (UHV), we demonstrate a new method for rapid crystallization of ASW *via* ACN diffusion–desorption induced porosity in the ASW matrix even in the window of 128–134 K, well below the normal crystallization temperature of 155 K. By placing an HDO (5% D_2O in H_2O) probe layer in ASW, we found that when ACN diffuses and desorbs through ASW, it induces ASW crystallization where the crystal grows both from the top and from the bottom simultaneously into the bulk. Crystallization kinetics and activation energy (E_a) for the formation of crystalline ice (CI) were evaluated using the Avrami equation and were compared with the previous reports. The evaluated E_a was ~53 kJ mol^{-1}, close to the E_a of crystal growth (47–56 kJ mol^{-1}) and it suggested the absence of a nucleation process and supported rapid crystallization. Such occurrence of CI due to diffusion of ACN suggests a possible mechanism for the former's existence in many astrophysical environments.

Introduction

A metastable form of solid water, ASW can be created by deposition of water vapour on a cold substrate below 130 K. The properties of ASW are of great importance for several reasons, including its use as a model for supercooled liquid water and in the context of astrophysical and planetary science.[1–4] Upon annealing, ASW gets converted to a metastable cubic CI at temperatures above 130 K, and a stable hexagonal CI at temperatures above 155 K in ultrahigh vacuum (UHV).[5] CI can also be formed by several other methods such as dissociation of clathrate hydrates,[6–10] sublimation/desorption of volatile molecules from the ice matrix,[11,12] and addition of neutral/acidic impurities into ASW.[13–18] The kinetics and mechanisms of ASW to CI transition have been investigated in several studies using various methods including temperature-programmed desorption, electron diffraction and infrared spectroscopy.[3,4,13,19–26] Most of these studies suggested that ASW crystallization initiates at random nucleation sites in the bulk and expands in all directions, although, a few reported that nucleation may commence at the ASW–vacuum interface.[27,28] However, Yuan *et al.*[22] by placing an HDO (5% D_2O in H_2O) layer at specific positions in an ASW film (1000 ML) confirmed that ASW crystallization in vacuum proceeds by a "top-down" crystallization mechanism and suggested that the higher mobility of surface molecules compared to those in bulk is the reason for preferential nucleation at ASW–vacuum.

Water being ubiquitous, even in space, the diffusion of volatile molecules existing in space and consequently deposited on ASW at cryogenic temperatures can affect the chemistry of interstellar grains. Fundamental processes on dust grains are adsorption, desorption, diffusion, and reaction, which depend significantly on the morphology of ASW.[5,29] While ASW is the predominant form of water in the interstellar medium, crystalline ice (CI) has also been detected within many astrophysical environments.[30–32] However, there is a lack of mechanistic information on the formation of CI in such conditions. Along with water, more than 240 molecules have been detected in the interstellar and circumstellar medium.[33] Hence, the interactions of volatile molecules on top and within water-rich ices are of fundamental importance in understanding many interstellar processes.[34]

Diffusion of reacting atoms and molecules[35] is essential for the chemical evolution of interstellar ices and has been studied

[a] *DST Unit of Nanoscience (DST UNS) and Thematic Unit of Excellence (TUE), Department of Chemistry, Indian Institute of Technology Madras, Chennai 600036, India*
[b] *Department of Chemistry, Mar Ivanios College, Thiruvananthapuram, Kerala 695015, India*
[c] *International Centre for Clean Water, IIT Madras Research Park, Chennai 600113, India. E-mail: pradeep@iitm.ac.in*

† Electronic supplementary information (ESI) available: Experimental section, isothermal time-dependent RAIRS spectra and TPD-MS spectra of pure ACN, ACN@ASW and ASW@ACN films, crystallization parameters of ASW at different temperatures. See DOI: https://doi.org/10.1039/d2cp02640f

previously[36,37] (and references therein). The main focus of diffusion studies (of volatile species) was to elucidate the diffusion–desorption kinetics of volatile molecules and how it is affected by the ASW structure. A distinct mechanism for the release of trapped gases (Ar, Kr, Xe, CH_4, N_2, O_2, or CO) from underneath the ASW films has been demonstrated in their low (1 monolayer) and high coverage (5 monolayers) regimes.[38,39] For low coverages of volatile species, the release mechanism is controlled by crystallization-induced cracks formed in the ASW overlayer. On the other hand, for the high coverage regime, two desorption pathways were suggested; the first occurs between 100–150 K and is due to pressure-induced structural failure of the ASW overlayer. The second pathway occurs at a low temperature below 100 K and is attributed to the diffusion through pores formed during ASW deposition. However, there is a lack of clarity on the effect of diffusion of volatile molecules on the structure of ASW. Here, we have investigated the effect of diffusion of ACN on the structure of ASW.

The ACN–water system has been studied from different perspectives such as adsorption/desorption of ACN on the top of ASW/crystalline ice surfaces, interactions with water and thermal processing of ACN and water ice.[12,40–45] However, to the best of our knowledge, multilayer ACN diffusion in ASW in ultrahigh vacuum conditions has not been explored yet. ACN has been detected in molecular clouds Sgr B and Sgr A[46] and comet Kohoutek[47] and is an important precursor of nitrogen-containing complex organic molecules including amino acids and nucleobases. Hence, the study of the diffusion of ACN in ASW will be of importance for planetary science, astrochemistry, and physical chemistry.

In the current work, we have studied the diffusion of ACN molecules in ASW from the top as well as beneath the ASW films and the consequence of this process on the structure of ASW in a narrow temperature window of 128–134 K, where systematic changes occur. While diffusion and desorption of ACN were monitored by temperature-programmed desorption mass spectrometry (TPD-MS), and Cs^+ ion based secondary ion mass spectrometry (SIMS), change in the ASW structure and the associated kinetics were investigated by reflection absorption infrared spectroscopy (RAIRS). We observed that when ACN diffuses in ASW from the top as well as underneath the ASW film, the process induces crystallization of the latter even at low temperatures well below the normal crystallization temperature of 155 K.

Experimental section

Experimental setup

All the experiments were carried out using the setup described elsewhere.[48] Briefly, the setup consists of a stainless steel UHV chamber, with a base pressure of $\sim 5 \times 10^{-10}$ mbar at room temperature. The vacuum chamber is equipped with reflection absorption infrared spectroscopy (RAIRS), temperature-programmed desorption (TPD) mass spectrometry, secondary ion mass spectrometry (SIMS), and low energy ion scattering (LEIS) mass spectrometry of mass-selected ions. The set-up has been used extensively to study molecular solids.[6,7,12,49,50] UHV was maintained by using several turbomolecular pumps backed by oil-free diaphragm pumps (Pfeiffer Vacuum). Pressure was monitored by a Bayard-Alpert gauge (Pfeiffer Vacuum), controlled by a MaxiGauge controller (Pfeiffer, Model TPG 256 A). A highly polished Ru(0001) single crystal was used as the substrate and was maintained at low temperature using a closed-cycle helium cryostat (ColdEdge Technologies). The substrate (1.5 cm diameter and 1 mm thick) was mounted on a copper holder and connected to the cold tip of the He cryostat. With the help of different thermal sensors (K-type thermocouple and a platinum sensor) and a resistive heater (25 Ω), the substrate temperature could be varied in the range of 8–1000 K with a temperature accuracy/uncertainty of 0.5 K. Temperature (ramping) was controlled and monitored with a temperature controller (Lakeshore, Model 336).

Sample preparation

Before preparing each sample, the Ru(0001) substrate was heated to 400 K multiple times to ensure the cleanness of the surface. Thin films of ices were created by vapour deposition at 10 K. Before vapour deposition, ACN (Merck, 99.9%), and Millipore water (H_2O of 18.2 MΩ resistivity) were taken in a vacuum-sealed test tube and further purified by several freeze-pump-thaw cycles. During the introduction of ACN and H_2O vapour to the UHV chamber, purity was further confirmed by the presence of their distinctive molecular ion peaks using a residual gas analyzer that was sensitive to a partial pressure of $\sim 10^{-10}$ mbar. Two sample lines were connected to the UHV chamber through a high-precision all-metal leak valve and directed to the middle of the substrate. Out of two sample lines, one was used exclusively for ACN and the other was used exclusively for water vapour deposition. The molecular deposition was controlled through the leak valves and coverage was expressed in monolayers (ML) assuming 1.33×10^{-6} mbar s = 1 ML, which was estimated to have $\sim 1.1 \times 10^{15}$ molecules cm^{-2}, as suggested in several reports.[50–52]

Experimental procedure

Diffusion of ACN in ASW was studied by creating layered ice thin films of ACN and H_2O by varying the position of the ACN layer. In one set of experiments, ACN films were deposited on Ru(0001) followed by ASW films (ACN film underneath ASW film, hereafter referred to as ACN@ASW) and in the second set of experiments, ASW films were deposited on Ru(0001) followed by ACN films (ACN film on top of ASW film, hereafter referred to as ASW@ACN). These ice films were prepared sequentially at 10 K by backfilling the vacuum chamber with ACN/H_2O vapours at a total pressure of $\sim 5 \times 10^{-7}$ mbar, starting from a base vacuum of $\sim 5 \times 10^{-10}$ mbar. Here, exposures were measured as the product of the dosing time and the chamber pressure of exposure.[45,51,52] For 50 ML of ACN film, the inlet pressure was kept at $\sim 5 \times 10^{-7}$ mbar for 1 min 40 s and for 150 ML of ASW film, the inlet pressure was $\sim 5 \times 10^{-7}$ mbar for 5 min. For other thicknesses of ACN and ASW films, the time of vapour

exposure to the vacuum chamber was varied accordingly. During sequential deposition, after the deposition of the first gas, we have waited sufficient time to get back the base pressure before the deposition of the second gas. Further, the as-deposited ice films were heated to the set temperatures at a rate of 2 K min^{-1}. Once a particular temperature was reached, the ice samples were investigated by RAIRS, TPD, and SIMS (additional experimental details are given in the ESI†).

Results and discussion

Diffusion of ACN in ASW

The diffusion of ACN in ASW was examined mainly by TPD-MS and SIMS experiments. Pure ACN desorbs at ~139 K as shown in Fig. S1a (ESI†) (RAIRS data) and S1b (TPD-MS data). Fig. 1a shows the TPD-MS spectrum of 200 ML of ACN@ASW (with 50 ML of ACN deposited first followed by 150 ML ASW over it) film with a heating rate of 10 K min^{-1}. The peak at 142 K is attributed to the bulk desorption of ACN through ASW. This abrupt desorption is due to a pressure-induced structural change in the ASW overlayer.[39] The marked region 1 (in the 120–130 K range), shows an initial (small) desorption of ACN which is attributed to the diffusion of ACN through pores formed during ASW deposition.[39] During ACN diffusion through ASW, a fraction of ACN will trap in ASW which may desorb along with H_2O above 150 K. The marked region 3 (in the range 150–160 K) shows trapped ACN desorption. So, Fig. 1a shows that the diffusion and desorption of ACN from underneath ASW will start below 120 K, and accelerates above 130 K giving a desorption maximum at 142 K. Similarly, Fig. 1b shows the TPD-MS spectrum of 200 ML of ASW@ACN (with 150 ML of ASW and 50 ML of ACN over it) film with a heating rate of 10 K min^{-1}. The peak at 139 K is due to the bulk desorption of

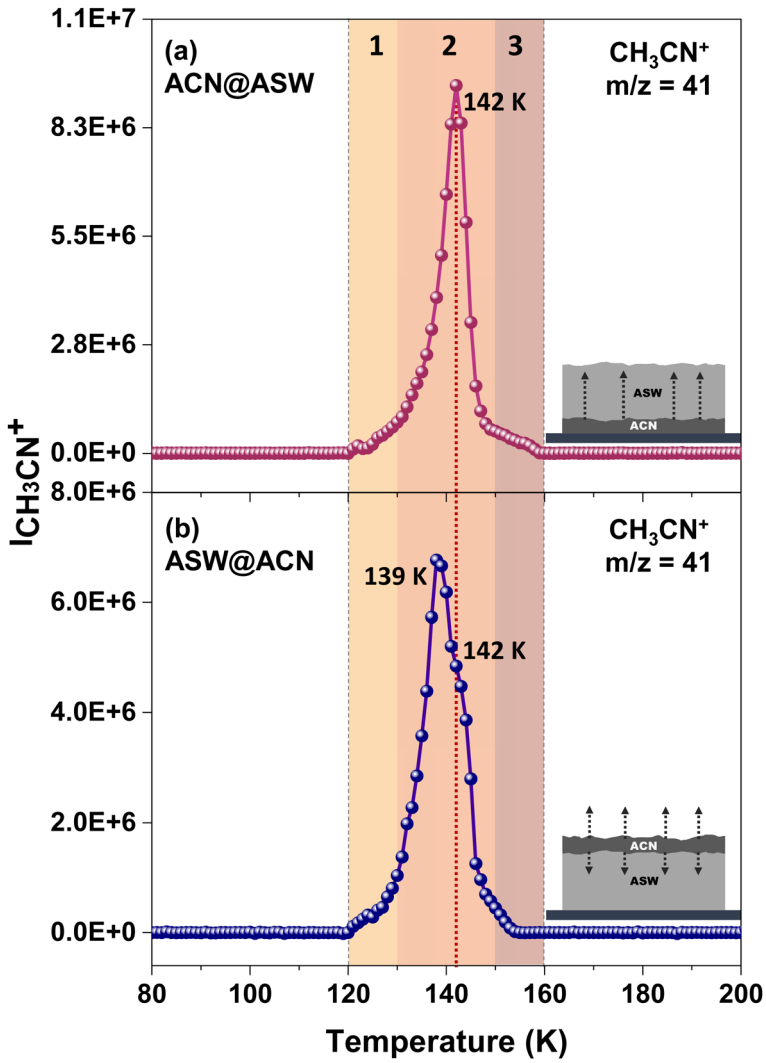

Fig. 1 Desorption of 50 ML of ACN from 150 ML of ASW during 10 K min^{-1} TPD experiments. The marked region 1 indicates initial ACN desorption at 120–130 K, the region 2 shows bulk ACN desorption at 130–150 K and the region 3 shows trapped ACN desorption at 150–160 K. (a) TPD-MS spectra of 200 ML of ACN(50 ML)@ASW(150 ML). (b) TPD-MS spectra of 200 ML of ASW(150 ML)@ACN(50 ML). The inset pictures in (a) and (b) show the composition of sequentially deposited ACN and ASW films on Ru(0001) at 10 K and the dotted arrows show the diffusion and desorption path of ACN.

ACN from ASW surface and is similar to the desorption of pure ACN from the Ru(0001) substrate, as shown in Fig. S1b (ESI†). The shoulder at 142 K, in Fig. 1b, is assigned to the desorption of a fraction of ACN that diffused into ASW and returned to the surface as temperature was raised. This assignment is reasonable as this shoulder coincides with the peak at 142 K in Fig. 1a which is due to the desorption of ACN that diffuses through ASW. This was further confirmed in a separate experiment where instead of the ASW layer we have taken a crystalline H_2O layer. TPD-MS data in Fig. S2a (ESI†) shows the desorption of 50 ML of ACN from the surface of 150 ML of crystalline H_2O. The absence of a shoulder at 142 K in Fig. S2a (ESI†) suggests that ACN could not diffuse into crystalline H_2O but desorbed at 140 K, similar to pure ACN desorption from the Ru(0001) substrate. These observations confirm that the shoulder at 142 K in Fig. 1b is due to a fraction of ACN that diffuses into ASW. In summary, when ACN was underneath ASW, it diffuses through ASW with a single desorption feature at 142 K, whereas when ACN was deposited on top of ASW, it desorbed with two desorption features where one coincides with pure ACN desorption at 139 K and the second coincides with the peak at 142 K, as in Fig. 1a. As the intensities of the peaks at 139 and 142 K are at a $\sim$7 : 3 ratio we conclude that about $\sim$30% of the ACN deposited diffuses into ASW and desorbs subsequently (Fig. S2b, ESI†).

To get a clearer picture of ACN diffusion in ASW, we have done SIMS experiments (see the experimental details in ESI†) on ACN@ASW, and ASW@ACN films. Here we have used the Cs^+ scattering technique, which is versatile to probe the topmost layer of solid surfaces.[53–55] We note that Cs^+ scattering at low energies is sensitive only to the first few layers of the surface. In the mass spectra shown in the Fig. 2, the peaks at m/z 151, 169 and 174 correspond to the adduct of Cs^+ (m/z 133) with H_2O ($Cs(H_2O)^+$, $Cs(H_2O)_2{}^+$) and ACN ($Cs(CH_3CN)^+$), respectively. Fig. 2a shows a series of mass spectra for 200 ML of ACN@ASW (with 50 ML of ACN and 150 ML of ASW) film in the window of 10–150 K. Inset in each panel shows an expanded view in the m/z 170–178 window to see the evolution of $Cs(CH_3CN)^+$ peak. At 10–100 K, we could observe only H_2O (m/z 151) at the sample surface; although, at 110 K, we noted a small peak at m/z 174 along with a peak at m/z 151. This peak at m/z 174 suggests that a small fraction of ACN has diffused through ASW and reached the surface. The intensity of the peak at m/z 174 increased subsequently with temperature (up to 140 K), owing to the diffusion of a larger fraction of ACN to the surface. At 150 K, m/z 174 disappeared and only water peaks (m/z 151, and 169) were present. Fig. 2b shows a series of mass spectra for 200 ML of ASW@ACN (with 150 ML of ASW and 50 ML of ACN) film. At 10–90 K, only ACN (m/z 174) was observed, but at 100 K, we observed a small peak at m/z 151 along with another at m/z 174. This suggests the commencement of diffusion of ACN in ASW as well as H_2O diffusion from the bottom, to the topmost surface. With an increase in substrate temperature from 100–140 K, the intensity of the peak at m/z 151 has increased and that of the peak at m/z 174 has roughly maintained the same intensity. At 140 K, the peak at m/z 174 confirms ACN diffusion in ASW. If ACN could not have diffused into ASW, we would have seen a decrease in the peak intensity at 140 K. We understand that when ACN does not diffuse into CI, it desorbed at 140 K as shown in TPD-MS results (Fig. S2a, ESI†). At 150 K, the peak at m/z 174 has vanished (Fig. 2b) and, a new peak at 169 ($Cs(H_2O)_2{}^+$) along with a peak at m/z 151 was observed. In summary, the results of SIMS experiments in Fig. 2, along with the TPD-MS data suggest that when the ACN film was underneath ASW, it diffused through the pores of ASW and reached the surface even at 110 K, whereas, when ACN film was on top of ASW, a fraction of ACN deposited diffused into ASW and remained in the sample even at 140 K.

In the next sections, we will discuss the impact of ACN diffusion on ASW structure with the help of RAIRS experiments.

Effect of ACN diffusion on ASW structure

In our previous report[12] on ACN–ASW system, we examined the composition-dependent phase separation of ACN and H_2O, and associated structural changes in the ASW matrix. We observed that co-deposited ACN and H_2O films (in 1 : 1, 1 : 5 and 5 : 1 ratios), when isothermally annealed at 125–135 K resulted in crystalline ice after ACN desorption. In interstellar and cometary ices, the molecular components are embedded in or frozen on top of the water ice, depending on the cosmochemical history of the ice. Therefore, studying the behaviour of water–ice in the sandwich (ACN@H_2O) and mixed (ACN:H_2O)[12] films upon ACN release is of greater significance. Therefore, in this paper, we monitored the diffusion of multilayer ACN into the bulk of ASW in the sandwich (ACN@ASW and ASW@ACN) films, and studied the consequence of this process on the ASW matrix systematically. For this, we deposited ACN and ASW sequentially at 10 K and heated the sample at a rate of 2 K min^{-1} to the desired temperatures and IR spectral evolution was monitored subsequently. These experiments were done by varying ACN thickness (50–150 ML) in ACN@ASW and ASW@ACN films while keeping ASW thickness constant at 150 ML. During annealing from 10–133 K, a small fraction of ACN could have already diffused and desorbed through ASW (TPD-MS data, Fig. 1). At 133 K, the remaining ACN diffused and desorbed from the ACN@ASW and ASW@ACN films within 30 and 60 min, respectively (the spectral change in the C$\equiv$N stretching region with time can be seen in Fig. S3a and b, ESI†). We suppose that the ASW films after diffusion followed by desorption of ACN are highly porous. The porosity could range from microporosity to cracks of macroscopic dimensions. It is not possible to examine the pore size distribution of ASW by IR spectroscopy alone.[37] However, the O–H stretching band shows a major change after the diffusion and desorption of ACN from ASW (Fig. S4a–d and S5a–d, for ACN@ASW and ASW@ACN films, respectively, ESI†). For example, for 200 ML of ACN@ASW (50 ML ACN and 150 ML of ASW) film, in Fig. 3a; the first, broad spectrum (orange curve) at 0 min corresponds to the entirely amorphous nature of the sample, whereas, the last spectrum (blue curve) obtained after 130 min is attributed to the complete crystallization of ASW.[13,27] The obtained peak

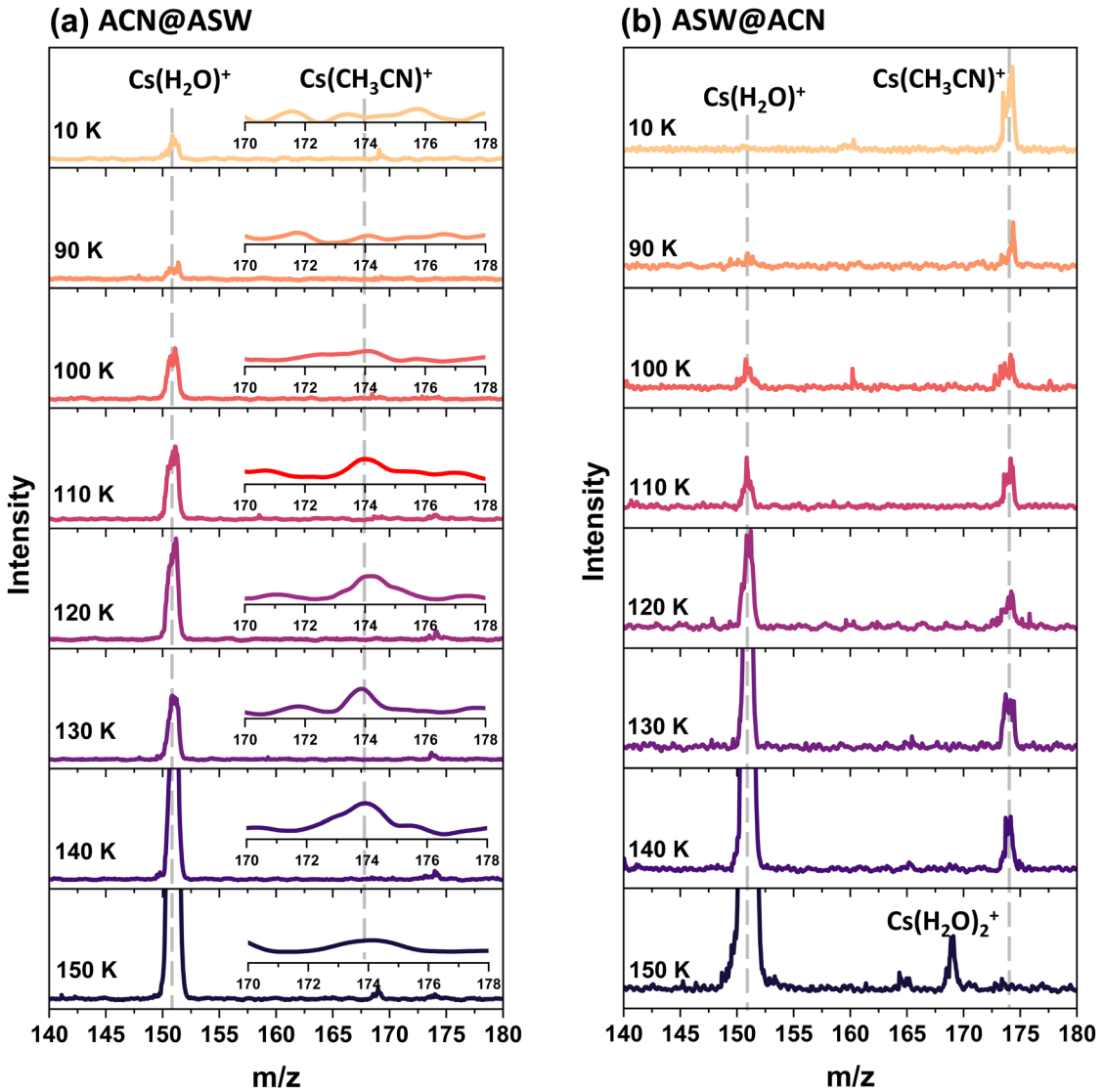

Fig. 2 Cs^+ scattering mass spectra of sequentially deposited ice layers of ACN and ASW. Deposited ices were collided with 120 eV Cs^+ ions at 10–150 K. The mass spectra contain peaks corresponding to adducts of Cs^+ ions with ACN and H_2O. The ions observed in mass spectra are Cs^+ (*m*/*z* 133) (not shown here), $Cs(H_2O)^+$ (*m*/*z* 151), $Cs(H_2O)_2^+$ (*m*/*z* 169), $Cs(CH_3CN)^+$ (*m*/*z* 174). (a) Mass spectra of ACN(50 ML)@ASW(150 ML) in the *m*/*z* range of 140–180 at 10–150 K, where inset plots in each panel are expanded spectra in the *m*/*z* range of 170–178 to see the evolution of $Cs(CH_3CN)^+$. (b) Mass spectra of ASW(150 ML)@ACN(50 ML), in the *m*/*z* range of 140–180 at 10–150 K where evolution of adducts of Cs^+ ions with ACN and H_2O were monitored.

shape and bands correspond to the hexagonal ice (ice I_h) (Fig. S6a, ESI†).[7,12] We will refer it as CI. In our previous reports,[6,7,12] we have seen that 150 ML of ASW cannot undergo crystallization at 120–135 K in similar experimental conditions (result of isothermal annealing of ASW at 133 K for several hours is shown in Fig. S6b, ESI†). This suggests that ACN diffusion in ASW has induced ASW crystallization.

Fig. 3b shows the combined crystallization fraction (CF) *versus* time curves for ACN@ASW (solid lines with square) and ASW@ACN (dished line with circle) films obtained from the RAIRS measurement at 133 K from a vertical cut at 3260 cm^{-1} in the O–H stretching band shown in Fig. S4a–d and S5a–d (ESI†). The ACN film with different thicknesses is shown in different colours (for example, 50 ML of ACN is shown in orange and 150 ML in blue). Fig. 3b shows that the crystallization kinetics is faster and independent of ACN film thickness when ACN diffuses and desorbs from underneath ASW (solid lines with square) compared to the case when ACN diffuses and desorbs from the top of ASW (dished line with circle) where crystallization kinetics is slower and increases with increase in ACN film thickness from 50–150 ML. If we compare the crystallization half-time (the time at which the CF = 0.5) the former took ~2080 s whereas the latter took ~5260 s for 50 ML of ACN with 150 ML of ASW. In the former case, the crystallization kinetics is roughly independent of ACN thickness (50–150 ML). We suggest that after the initial diffusion and desorption of a fraction of ACN through ASW, the latter possesses sufficient pores and cracks to release the

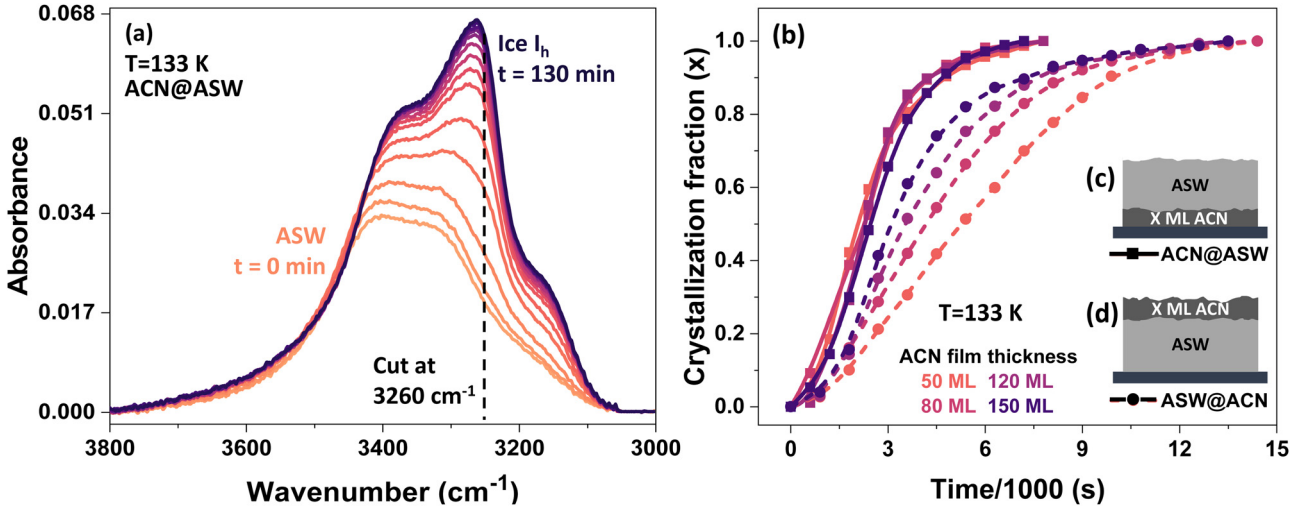

Fig. 3 (a) Time-dependent RAIRS spectra of 200 ML of ACN@ASW film at 133 K in the O–H stretching region. The film was sequentially deposited on Ru(0001) at 10 K and heated at a rate of 2 K min^{-1} to 133 K. The yellow curve (at 0 min) is the spectrum from complete amorphous film and blue curve (at 130 min) is the spectrum for a complete crystalline film. The vertical cut at 3260 cm^{-1} was utilized to determine the CF. (b) Combined CF *versus* time curves for ACN@ASW (solid lines with square) and ASW@ACN (dished line with circle) films with varying ACN film thickness (50–150 ML) while keeping ASW film thickness constant at 150 ML. CF was obtained from isothermal RAIRS measurements at 133 K. The CF was calculated from a vertical cut at 3260 cm^{-1} in the O–H stretching band for the time-dependent RAIRS spectra shown in Fig. S4a–d (ESI†) (for ACN@ASW) and Fig. S5a–d (ESI†) (for ASW@ACN). (c and d) Composition of sequentially deposited ACN and ASW films on Ru(0001) at 10 K.

remaining ACN through it without much perturbation. To prove this, additionally, we examined the critical thickness of ACN layers required to induce ASW crystallization, for which we have placed 10, 20, and 30 ML of ACN layers below 150 ML of ASW and found that 30 ML of ACN is sufficient to induce ASW crystallization at 133 K (Fig. S7, ESI†). This is why the kinetics of ASW crystallization is almost similar for films containing 50–150 ML of ACN. While, in the latter case, crystallization increases with an increase in ACN film thickness. We propose that, as the ACN film thickness increases, the extent of diffusion of ACN in ASW also increases. This suggests that the more the diffusion of ACN in ASW, the higher will be the porosity, in turn, the faster will be the kinetics of crystallization. Thus, the results of Fig. 3 suggest that the diffusion of ACN in ASW is crucial for the commencement of ASW crystallization.

However, the differences in ASW crystallization kinetics for ACN@ASW and ASW@ACN films were thought to be due to a different crystallization mechanism that is involved in the process and this was investigated by placing HDO (5% D_2O in H_2O) probe layers in ASW. This methodology for investigating the crystallization mechanism was used before.[13,22]

In separate experiments, we have embedded 50 ML of HDO probe layer in the ACN@ASW and ASW@ACN films at specific positions as shown in the inset pictures in Fig. 4a and b, and evaluated the CF at 133 K by monitoring the evolution in the O–D stretching band of HDO (Fig. S8 and S9, ESI†) as a function of time of crystallization. Fig. 4 shows the change in the CF of the HDO layer embedded at different locations; near the ACN layer (yellow curve), 50 ML away from ACN layer (brown curve) and 100 ML away from the ACN layer (blue curve) in the sample. These 50 and 100 ML spacer layers were made of ASW. Fig. 4a shows that the HDO layer close and distant to the ACN layer crystallized first and almost at the same speed while the HDO layer embedded in the middle of the ASW crystallized later. This implies that diffusion of ACN from underneath ASW induced crystal growth both from the top and bottom simultaneously and the crystallization propagated from both directions into the bulk of ASW. Such an effect of diffusion of volatile gases on the ASW structure appears to be seen for the first time. The reason for such a mechanism is (1) at the ACN–ASW interface the required mobility for H_2O rearrangement to CI is obtained from the release of 50 ML of ACN through the ASW. This pressure-induced structural change in ASW due to ACN release will be maximum at the ACN–ASW interface compared to the bulk, (2) at the ASW–vacuum interface during annealing of the sample, ACN will diffuse through ASW and reach the surface before desorbing. The ASW films after diffusion followed by desorption of ACN are expected to be highly porous. The increased porosity consequently means more surface area and the formation of pre-crystallization nuclei[56,57] is more facile on the surface than in the bulk.

In contrast, in Fig. 4b the CF of the HDO embedded ASW@ACN films shows that the HDO layer closer to the ACN layer crystallized first followed by the middle and distant layers. This implies that the crystal growth has started at the ACN–ASW interface and propagated through the interior of ASW. If we see closely, the HDO layer which was placed in the middle, crystallized roughly along with the HDO layer near the ACN layer. This is because a small fraction of ACN diffused tens of ML into the ASW during isothermal annealing (confirmed with TPD and SIMS data, above). Diffusion and desorption of these ACN molecules will create more porosity in ASW as discussed above and subsequently will increase the speed of crystallization.

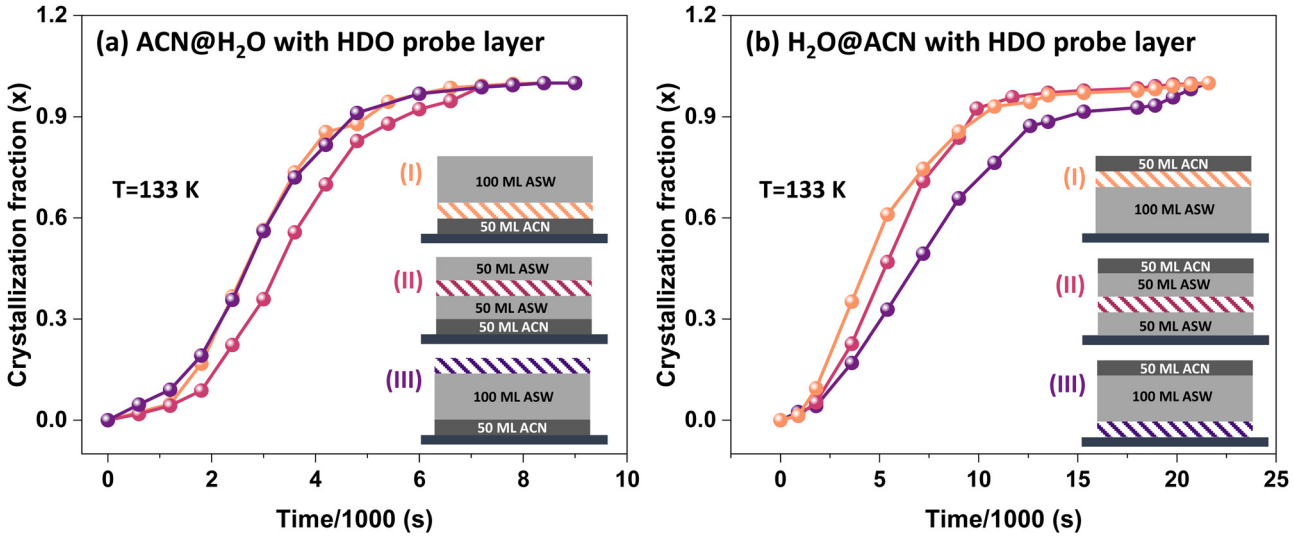

Fig. 4 The CF *versus* time curves for (a) ACN@H_2O, and (b) H_2O@ACN films with HDO (5% D_2O in H_2O) layer, obtained from isothermal RAIRS measurements at 133 K where a 50 ML of HDO layer was embedded at various positions in the ASW. The HDO layer is indicated by colored pattern in the inset pictures; HDO layer near ACN (0 ML away), 50 ML away, and 100 ML away from ACN layer are shown by (I) orange, (II) brown and (III) blue patterns, respectively. ASW layer is indicated by light grey. The colors of the obtained curves are shown by the corresponding colors. The CF was calculated from a vertical cut at 2424 cm^{-1} in the O–D stretching band for the time-dependent RAIRS spectra shown in Fig. S8a–c and S9a–c (ESI†). ACN layer thickness was 50 ML.

When the ACN layer was on top of the ASW layer, it is clear that the crystallization had started at the surface and propagated into the interior and had slower kinetics as shown in Fig. 4b. But, when ACN was placed underneath ASW (Fig. 4a), we propose that the onset of crystallization was happening from top and bottom simultaneously and this was the reason for faster crystallization kinetics. To confirm whether crystallization had started at surfaces (or interfaces) or in the bulk, we have conducted thickness dependent experiments with ASW. As demonstrated in the previous reports[13,58,59] if nucleation occurs in bulk ASW, crystallization takes place faster in thicker ASW film than in thinner film whereas if crystallization initiates at the surface of the ASW film, it takes longer for a thicker film than in a thinner film. Fig. S10 (ESI†) shows the CF *versus* time curves for the ACN@ASW films with varying ASW film thickness (50–200 ML), obtained from isothermal RAIRS measurements at 133 K, keeping the ACN film thickness constant at 50 ML (Fig. S11, ESI†). We found that ASW with 50–100 ML thickness crystallizes faster than those with 150, 200 ML. Following the above arguments, these results suggest that crystallization has started at the surface and not in the bulk.

Thus, the results of Fig. 4 answer the question of the large difference in the ASW crystallization kinetics for ACN@ASW and ASW@ACN films, as shown in Fig. 3b. Faster kinetics in the former case is attributed to the crystal growth from the top and bottom simultaneously unlike in the latter case, where crystal growth propagates only from the top and required more time.

It should be noted that ASW overlayers grown over underlayer amorphous ACN, crystalline ACN films, and Ru(0001) substrate will have different porosities.[39] To examine this effect, 150 ML of ASW was grown over 50 ML of amorphous ACN, 50 ML of crystalline ACN, and bare Ru(0001) substrate. The resulting ices were annealed at 133 K isothermally, and the RAIRS spectra collected are presented in Fig. S12a, c and S6b (ESI†). Fig. S6b (ESI†) shows ASW grown over Ru(0001) substrate, which does not undergo crystallization at 133 K even after 6 h. Fig. S13 (ESI†) shows the crystallization fraction *versus* time curve, obtained from the RAIRS spectra presented in Fig. S12 (ESI†). The results suggest that the ASW grown over amorphous ACN crystallizes faster than when it was prepared over crystalline ACN. Following the above observation, we suggest that the ASW grown over amorphous ACN might have more porosity than when it was grown over Ru(0001) substrate or crystalline ACN film. The porosity might further increase due to the ACN burst above 130 K (Fig. 1a), where ASW undergoes pressure-induced structural failure.[39,60]

Crystallization kinetics

Crystallization kinetics and related kinetic parameters of ASW crystallization were evaluated using time-dependent RAIRS spectra[6,7,12,13,24] under isothermal conditions at the corresponding temperatures, 128–134 K for the ACN@ASW film. As prepared ACN@ASW (with 50 ML of ACN and 150 ML of ASW) films at 10 K were annealed to the set temperatures and RAIRS spectra were recorded as a function of time. Fig. S14a–d (ESI†) shows the O–H stretching region for ACN@ASW films and were utilized to evaluate the crystallization kinetics. All the spectra shown in Fig. S14 (ESI†) have an isosbestic point, which indicates that the absorbance is due to the contributions of two states, amorphous and crystalline. In Fig. 5a, the first spectrum (t = 0 min, orange trace) is due to the completely amorphous film and the final spectrum (t = 200 min, blue trace) is from the completely crystalline film. The intermediate spectra represent

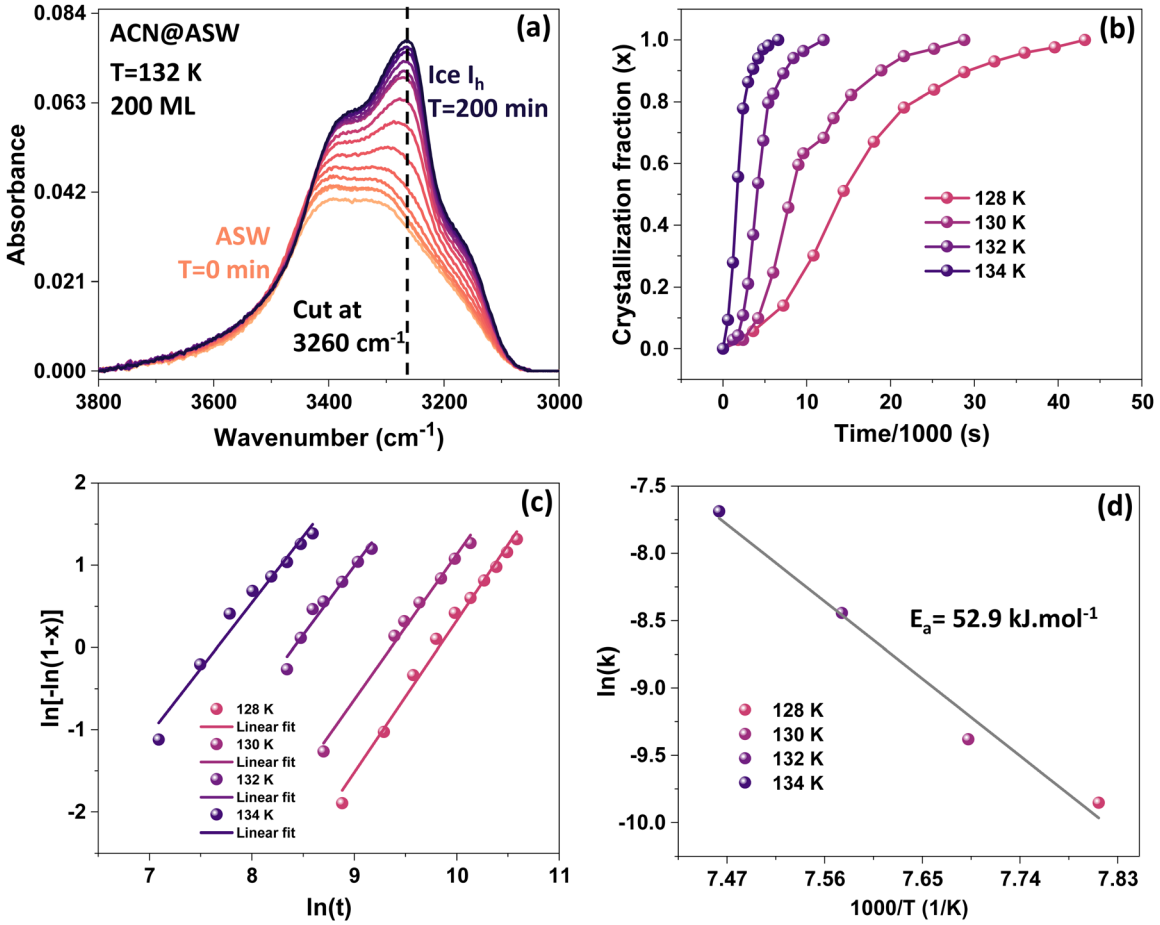

Fig. 5 (a) Time-dependent RAIRS spectra of 200 ML of ACN@ASW film at 132 K in the O–H stretching region. The film was sequentially deposited on Ru(0001) at 10 K and heated at a rate of 2 K min^{-1} to 132 K. (b) CF *versus* time curves for 200 ML of ACN@ASW film obtained from isothermal RAIR measurements at 128, 130, 132 and 134 K. The fraction crystallized *versus* time was calculated from a vertical cut at 3260 cm^{-1} in the O–H stretching band for a set of time-dependent RAIRS spectra shown in Fig. S14a–d (ESI†). (c) A plot of the linearized form of the Avrami equation for ASW crystallization. Plots of ln(−ln[1 − *x*]) *versus*. ln (*t*) at different temperatures of 128, 130, 133, and 134 K were evaluated using the O–H stretching bands. The obtained data points were fitted using the Avrami equation. (d) Arrhenius plot of ln *k versus* (1/*T*), achieved from the analysis of the slope and intercept of the linearly fitted lines of plot (c) for different temperatures. The activation energy (E_a) of ice crystallization was calculated from the slope of the linearly fitted straight line of plot (d).

the progress of crystallization and are a combination of amorphous and crystalline spectra. The fraction crystallized with time can be calculated at a fixed wavenumber (3260 cm^{-1}) by subtracting the spectrum obtained at 0 min from the spectrum obtained at time *t*, for each temperature. Fig. 5b shows the CF *versus* time curves for ACN@ASW films at 128–134 K, obtained from the isothermal RAIRS spectra, shown in Fig. S14 (ESI†). The CF(x) was calculated by eqn (1),

$$x(t) = \frac{\Delta A(1)}{\Delta A(2)} \quad (1)$$

where $\Delta A(1)$ is the difference in the absorbance at a particular time *t* and that at time zero of an ACN@ASW film, and $\Delta A(2)$ is the difference in absorbance of a completely crystallized film (when there is no further spectral change with time) and that of a completely amorphous film (at $t = 0$) at the given temperature.

It is evident from the change of the shape of curves in Fig. 5b that the speed of crystallization increases with increasing temperature. The nucleation and growth mechanism of ASW can be evaluated by fitting the CF to the Avrami equation.[61,62] The Avrami equation is given by,

$$x(t) = 1 - \exp(-k{\cdot}t)^n \quad (2)$$

where *t* is time, *k* is the crystallization rate constant, and *n* is the time exponent which predicts the crystallization mechanism. For all the temperatures, *n* can have an integer value between 1–4 where $n = 4$ suggests three-dimensional growth with random nucleation in the bulk. However, when nucleation occurs at the surface of a film and crystal growth is perpendicular to the surface, *n* becomes close to 1.[13,24,63] eqn (2) can be rearranged in a linear form.

$$\ln(-\ln[1 - x(t)]) = n \ln(t) + n \ln k \quad (3)$$

Fig. 5c shows a plot between ln(−ln[1 − $x(t)$]) and ln(t) for different temperatures and the plots were evaluated by using eqn (3). The value of *n* and *k* for different temperatures were

obtained from the linearly fitted lines, listed in Table S1 (ESI†). The obtained value of k in the current study (for ACN@ASW) is closer to our previous study (obtained from the co-deposited ACN and H_2O films)[12] and is larger than the previously reported values,[7,24] estimated in similar experimental conditions.

The estimated value of n from curve fitting was between 1.84 and 1.60. It reflects that the crystallization kinetics is diffusion-controlled with particles growing into a predominantly spherical geometry as the theory of phase transformation by nucleation and growth would suggest.[25,64,65] However, a lower value of n suggests a low dimensional growth and the direction of crystal growth is limited, namely perpendicular to the surface. It again proves that ASW crystallization in ACN@ASW film has started at the surface rather than in the bulk. This implies that the diffusion of ACN through ASW increases the mobility of H_2O molecules more at the interfaces (ASW–vacuum interface and ASW–ACN interface) compared to the bulk. It should be noted that the value of n cannot distinguish whether the crystallization is happening top-down or bottom-up. Fig. 5d shows an Arrhenius plot of $\ln k$ *versus* $(1/T)$, derived from the analysis of the slope and intercept of the linearly fitted lines of the plot (c) for different temperatures. The activation energy (E_a) of ASW crystallization was estimated to be $\sim$53.0 kJ mol^{-1} from the slope of the linearly fitted line in Fig. 5d. However, the activation energy for crystallization of pure ASW films was previously reported[13,24,63,66] between 60–77 kJ mol^{-1}. Several researchers[57,67] by decoupling the nucleation and growth kinetics of phase change suggested the energy barrier of the growth step to be 47–56 kJ mol^{-1}. Thus, the obtained E_a value in our results, 53.0 kJ mol^{-1} explains the dramatic acceleration of crystallization kinetics, where only the growth step was required for crystallization to occur. The lower activation energy in this report is attributed to the diffusion-induced crystallization of ASW. ACN being a larger molecule, its diffusion through the ASW can enhance the mobility of water molecules to overcome the crystallization barrier even at low temperatures, than its usual crystallization temperature.

Conclusions

We have studied the effect of diffusion of multilayer ACN on the structure of ASW and provided an associated mechanism for ASW crystallization. We observed that when the ACN layer is placed below ASW, it induces crystallization faster, compared to the case when ACN was placed at the top of ASW. The faster kinetics occurs because crystallization happens from the top and bottom of the ASW film simultaneously and propagates into the bulk. This suggests that the diffusion of ACN through ASW increases the mobility of H_2O molecules, more at the interfaces compared to the bulk. The crystallization kinetics and activation energy of ASW crystallization was estimated. Minimum ACN thickness to induce crystallization was found to be 30 ML for 150 ML of ASW. It is known that CI is found in many astrophysical environments and diffusion of molecules is a key process in the chemistry of interstellar ices. These findings will open a path for the study of molecular diffusion and its effects on ASW structure for several organic molecules of interstellar relevance.

Author contributions

T. P. proposed the project and supervised the progress. G. V. designed the experiments. G. V. and B. K. M. have performed the experiment. G. V., B. K. M., and R. R. J. M. have analysed the results. The manuscript was written with the contributions of all authors.

Conflicts of interest

The authors declare no competing financial interests.

Acknowledgements

We acknowledge the Science and Engineering Research Board (SERB), Department of Science and Technology (DST), Government of India for research funding. T. P. acknowledges funding from the Centre of Excellence on Molecular Materials and Functions under the Institution of Eminence scheme of IIT Madras. We thank Dr Bhalamurugan Sivaraman for his valuable comments and discussions. We also thank Soham Chowdhury for his contributions to this work. G. V. thanks IITM for his research fellowship. B. K. M. thanks the Council of Scientific & Industrial Research (CSIR) for his research fellowship.

References

1 C. A. Angell, Amorphous Water, *Annu. Rev. Phys. Chem.*, 2004, **55**, 559–583.
2 C. A. Angell, Insights into phases of liquid water from study of its unusual glass-forming properties, *Science*, 2008, **319**, 582–587.
3 P. Jenniskens and D. F. Blake, Structural Transitions in Amorphous Water Ice and Astrophysical Implications, *Science*, 1994, **265**, 753–756.
4 R. S. Smith, N. G. Petrik, G. A. Kimmel and B. D. Kay, Thermal and nonthermal physiochemical processes in nanoscale films of amorphous solid water, *Acc. Chem. Res.*, 2012, **45**, 33–42.
5 N. Watanabe and A. Kouchi, Ice surface reactions: A key to chemical evolution in space, *Prog. Surf. Sci.*, 2008, **83**, 439–489.
6 J. Ghosh, R. G. Bhuin, G. Vishwakarma and T. Pradeep, Formation of Cubic Ice via Clathrate Hydrate, Prepared in Ultrahigh Vacuum under Cryogenic Conditions, *J. Phys. Chem. Lett.*, 2020, **11**, 26–32.
7 J. Ghosh, G. Vishwakarma, S. Das and T. Pradeep, Facile Crystallization of Ice I_h *via* Formaldehyde Hydrate in

Ultrahigh Vacuum under Cryogenic Conditions, *J. Phys. Chem. C*, 2021, **125**, 4532–4539.
8 A. Falenty, T. C. Hansen and W. F. Kuhs, Cubic Ice Formation and Annealing during CO_2 Clathrate Hydrate Decomposition at Low Temperatures, *Phys. Chem. Ice*, 2010, 411.
9 A. Falenty and W. F. Kuhs, 'Self-Preservation' of CO_2 Gas Hydrates-Surface Microstructure and Ice Perfection, *J. Phys. Chem. B*, 2009, **113**, 15975–15988.
10 W. F. Kuhs, G. Genov, D. K. Staykova and T. Hansen, Ice perfection and onset of anomalous preservation of gas hydrates, *Phys. Chem. Chem. Phys.*, 2004, **6**, 4917–4920.
11 T. Hama, S. Ishizuka, T. Yamazaki, Y. Kimura, A. Kouchi, N. Watanabe, T. Sugimoto and V. Pirronello, Fast crystalline ice formation at extremely low temperature through water/neon matrix sublimation, *Phys. Chem. Chem. Phys.*, 2017, **19**, 17677.
12 G. Vishwakarma, J. Ghosh and T. Pradeep, Desorption-induced evolution of cubic and hexagonal ices in an ultra-high vacuum and cryogenic temperatures, *Phys. Chem. Chem. Phys.*, 2021, **23**, 24052–24060.
13 D. H. Lee and H. Kang, Acid-Promoted Crystallization of Amorphous Solid Water, *J. Phys. Chem. C*, 2018, **122**, 24164–24170.
14 S. M. McClure, E. T. Barlow, M. C. Akin, P. L. Tanaka, D. J. Safarik, T. M. Truskett and C. B. Mullins, Effect of dilute nitric acid on crystallization and fracture of amorphous solid water films, *J. Phys. Chem. C*, 2007, **111**, 10438–10447.
15 R. Souda, Effects of methanol on crystallization of water in the deeply supercooled region, *Phys. Rev. B: Condens. Matter Mater. Phys.*, 2007, **75**, 184116.
16 R. Souda, Crystallization of thin water films on graphite: Effects of *n*-hexane, formaldehyde, acetone, and methanol additives, *Appl. Surf. Sci.*, 2015, **357**, 1809–1815.
17 R. A. May, R. S. Smith and B. D. Kay, Probing the interaction of amorphous solid water on a hydrophobic surface: Dewetting and crystallization kinetics of ASW on carbon tetrachloride, *Phys. Chem. Chem. Phys.*, 2011, **13**, 19848–19855.
18 R. Souda, Probing surface properties and glass - Liquid transition of amorphous solid water: Temperature-programmed TOF-SIMS and TPD studies of adsorption/desorption of hexane, *J. Phys. Chem. B*, 2005, **109**, 21879–21883.
19 R. Souda and T. Aizawa, Crystallization kinetics of water on graphite, *Phys. Chem. Chem. Phys.*, 2018, **20**, 21856–21863.
20 R. A. May, R. S. Smith and B. D. Kay, Probing the interaction of amorphous solid water on a hydrophobic surface: Dewetting and crystallization kinetics of ASW on carbon tetrachloride, *Phys. Chem. Chem. Phys.*, 2011, **13**, 19848–19855.
21 P. Jenniskens and D. F. Blake, Crystallization of Amorphous Water Ice in the Solar System, *Astrophys. J.*, 1996, **473**, 1104–1113.
22 C. Yuan, R. S. Smith and B. D. Kay, Surface and bulk crystallization of amorphous solid water films: Confirmation of "top–down" crystallization, *Surf. Sci.*, 2016, **652**, 350–354.
23 P. Löfgren, P. Ahlström, J. Lausma, B. Kasemo and D. Chakarov, Crystallization kinetics of thin amorphous water films on surfaces, *Langmuir*, 2003, **19**, 265–274.
24 R. S. Smith, J. Matthiesen, J. Knox and B. D. Kay, Crystallization kinetics and excess free energy of H2O and D2O nanoscale films of amorphous solid water, *J. Phys. Chem. A*, 2011, **115**, 5908–5917.
25 W. Hage, A. Hallbrucker, E. Mayer and G. P. Johari, Crystallization kinetics of water below 150 K, *J. Chem. Phys.*, 1994, **100**, 2743–2747.
26 T. Kondo, H. S. Kato, M. Bonn and M. Kawai, Deposition and crystallization studies of thin amorphous solid water films on Ru(0001) and on CO-precovered Ru(0001), *J. Chem. Phys.*, 2007, **127**, 094703.
27 E. H. G. Backus, M. L. Grecea, A. W. Kleyn and M. Bonn, Surface crystallization of amorphous solid water, *Phys. Rev. Lett.*, 2004, **92**, 236101.
28 E. H. G. Backus and M. Bonn, Theory of bulk, surface and interface phase transition kinetics in thin films, *J. Chem. Phys.*, 2004, **121**, 1038.
29 T. Hama and N. Watanabe, *Chem. Rev.*, 2013, **113**, 8783–8839.
30 D. C. Jewitt and J. Luu, Crystalline water ice on the Kuiper belt object (50000) Quaoar, *Nature*, 2004, **432**(7018), 731–733.
31 F. Merlin, A. Guilbert, C. Dumas, M. A. Barucci, C. De Bergh and P. Vernazza, Properties of the icy surface of the TNO 136108 (2003 EL), *Astron. Astrophys.*, 2007, **466**, 1185–1188.
32 A. Omont, S. H. Moseley, T. Forveille, W. J. Glaccum, P. M. Harvey, L. Likkel, R. F. Loewenstein, C. M. Lisse, A. Omont, S. H. Moseley, T. Forveille, W. J. Glaccum, P. M. Harvey, L. Likkel, R. F. Loewenstein and C. M. Lisse, Observations of 40–70 Micron Bands of Ice in IRAS 09371 + 1212 and Other Stars, *Astrophys. J., Lett.*, 1990, **355**, L27.
33 B. A. Mcguire, 2021 Census of Interstellar, Circumstellar, Extragalactic, Protoplanetary Disk, and Exoplanetary Molecules, *Astrophys. J., Suppl. Ser.*, 2022, **259**, 30.
34 D. J. Burke and W. A. Brown, Ice in space: surface science investigations of the thermal desorption of model interstellar ices on dust grain analogue surfaces, *Phys. Chem. Chem. Phys.*, 2010, **12**, 5947–5969.
35 W. Tielens and A. G. G. M. Hagen, Model calculations of the molecular composition of interstellar grain mantles, *Astron. Astrophys.*, 1982, **114**, 245–260.
36 B. Maté, S. Cazaux, M. Á. Satorre, G. Molpeceres, J. Ortigoso, C. Millán and C. Santonja, Diffusion of CH 4 in amorphous solid water, *Astron. Astrophys.*, 2020, **643**, 163.
37 F. Mispelaer, P. Theulé, H. Aouididi, J. Noble, F. Duvernay, G. Danger, P. Roubin, O. Morata, T. Hasegawa and T. Chiavassa, Diffusion measurements of CO, HNCO, H_2CO, and NH_3 in amorphous water ice, *Astron. Astrophys.*, 2013, **555**, 13.
38 R. A. May, R. S. Smith and B. D. Kay, The release of trapped gases from amorphous solid water films. I. 'top–down' crystallization-induced crack propagation probed using the molecular volcano, *J. Chem. Phys.*, 2013, **138**(10), 104501.
39 R. Alan May, R. Scott Smith and B. D. Kay, The release of trapped gases from amorphous solid water films. II. "Bottom–up" induced desorption pathways, *J. Chem. Phys.*, 2013, **138**, 104502.

40 R. Gopi, N. Ramanathan and K. Sundararajan, Acetonitrile-water hydrogen-bonded interaction: Matrix-isolation infrared and ab initio computation, *J. Mol. Struct.*, 2015, **1094**, 118–129.
41 V. K. S. Bahr, Interaction of acetonitrile with thin films of solid water, *J. Chem. Phys.*, 2009, **130**, 214509.
42 R. Souda, Hydration–Dehydration of Acetonitrile and Methanol in Amorphous Solid Water, *J. Phys. Chem. C*, 2016, **120**, 934–943.
43 R. G. Bhuin, R. R. J. Methikkalam, B. Sivaraman and T. Pradeep, Interaction of Acetonitrile with Water–Ice: An Infrared Spectroscopic Study, *J. Phys. Chem. C*, 2015, **119**, 11524–11532.
44 J. E. Schaff and J. T. Roberts, Interaction of Acetonitrile with the Surfaces of Amorphous and Crystalline Ice, *Langmuir*, 1999, **15**, 7232–7237.
45 J. E. Schaff and J. T. Roberts, Toward an understanding of the surface chemical properties of ice: Differences between the amorphous and crystalline surfaces, *J. Phys. Chem.*, 1996, **100**, 14151–14160.
46 P. M. Solomon, K. B. Jefferts, A. A. Penzias and R. W. Wilson, Detection of Millimeter Emission Lines from Interstellar Methyl Cyanide, *Astrophys. J.*, 1971, **168**, L107.
47 B. L. Ulich and E. K. Conklin, Detection of methyl cyanide in Comet Kohoutek, *Nature*, 1974, **248**, 121.
48 S. Bag, R. G. Bhuin, R. R. J. Methikkalam, T. Pradeep, L. Kephart, J. Walker, K. Kuchta, D. Martin and J. Wei, Development of ultralow energy (1–10 eV) ion scattering spectrometry coupled with reflection absorption infrared spectroscopy and temperature programmed desorption for the investigation of molecular solids, *Rev. Sci. Instrum.*, 2014, **85**, 1–7.
49 R. R. J. Methikkalam, R. G. Bhuin, J. Ghosh, B. Sivaraman and T. Pradeep, Interaction of Acetonitrile with Alcohols at Cryogenic Temperatures, *J. Phys. Chem. C*, 2017, **121**, 2822–2835.
50 J. Ghosh, R. R. J. Methikkalam, R. G. Bhuin, G. Ragupathy, N. Choudhary, R. Kumar and T. Pradeep, Clathrate hydrates in interstellar environment, *Proc. Natl. Acad. Sci. U. S. A.*, 2019, **116**, 1526–1531.
51 H. Kang, T. H. Shin, S. C. Park, I. K. Kim and S. J. Han, Acidity of hydrogen chloride on ice, *J. Am. Chem. Soc.*, 2000, **122**, 9842–9843.
52 Y. Kim, E. Moon, S. Shin and H. Kang, Acidic Water Monolayer on Ruthenium(0001), *Angew. Chem.*, 2012, **124**, 12978–12981.
53 H. Kang, Chemistry of Ice Surfaces. Elementary Reaction Steps on Ice Studied by Reactive Ion Scattering, *Acc. Chem. Res.*, 2005, **38**, 893–900.
54 Y. Kim, E. S. Moon, S. Shin and H. Kang, Acidic water monolayer on ruthenium(0001), *Angew. Chem., Int. Ed.*, 2012, **51**, 12806–12809.
55 J. Cyriac, T. Pradeep, H. Kang, R. Souda and R. G. Cooks, Low-Energy Ionic Collisions at Molecular Solids, *Chem. Rev.*, 2012, **112**, 5356–5411.
56 D. J. Safarik and C. B. Mullins, A new methodology and model for characterization of nucleation and growth kinetics in solids, *J. Chem. Phys.*, 2003, **119**, 12510.
57 D. J. Safarik and C. B. Mullins, The nucleation rate of crystalline ice in amorphous solid water, *J. Chem. Phys.*, 2004, **121**, 6003–6010.
58 D. J. Safarik, R. J. Meyer and C. B. Mullins, Thickness dependent crystallization kinetics of sub-micron amorphous solid water films, *J. Chem. Phys.*, 2003, **118**, 4660.
59 D. J. Safarik and C. B. Mullins, Surface phase transformation kinetics: A geometrical model for thin films of nonvolatile and volatile solids, *J. Chem. Phys.*, 2002, **117**, 8110–8123.
60 A. Bar-Nun, J. Dror, E. Kochavi and D. Laufer, Amorphous water ice and its ability to trap gases, *Phys. Rev. B: Condens. Matter Mater. Phys.*, 1987, **35**, 2427–2435.
61 M. Avrami, Kinetics of phase change. I: General theory, *J. Chem. Phys.*, 1939, **7**, 1103–1112.
62 M. Avrami, Kinetics of phase change. II Transformation-time relations for random distribution of nuclei, *J. Chem. Phys.*, 1940, **8**, 212–224.
63 T. Kondo, H. S. Kato, M. Bonn and M. Kawai, Deposition and crystallization studies of thin amorphous solid water films on Ru(0001)and on CO-precovered Ru(0001), *J. Chem. Phys.*, 2007, **127**, 094703.
64 C. N. R. Rao and K. J. Rao, *Phase transitions in solids: an approach to the study of the chemistry and physics of solids*, McGraw-Hill, New York, 1978.
65 R. H. Doremus, *Rates of phase transformations*, Academic Press, New York, 1985.
66 C. Yuan, R. S. Smith and B. D. Kay, Communication: Distinguishing between bulk and interface-enhanced crystallization in nanoscale films of amorphous solid water, *J. Chem. Phys.*, 2017, **146**, 031102.
67 Z. Dohnálek, G. A. Kimmel, R. L. Ciolli, K. P. Stevenson, R. S. Smith and B. D. Kay, The effect of the underlying substrate on the crystallization kinetics of dense amorphous solid water films, *J. Chem. Phys.*, 2000, **112**, 5932–5941.

